MULTI-SPACECRAFT STUDY OF THE JANUARY 21, 2005 ICME

EVIDENCE OF CURRENT SHEET SUBSTRUCTURE NEAR THE PERIPHERY OF A STRONGLY EXPANDING, FAST, MAGNETIC CLOUD

C. FOULLON[1], C.J. OWEN[1], S. DASSO[2,3], L.M. GREEN[1], I. DANDOURAS[4], H.A. ELLIOTT[5], A.N. FAZAKERLEY[1], Y.V. BOGDANOVA[1], and N.U. CROOKER[6]

[1] *Mullard Space Science Laboratory, University College London, Holmbury St. Mary, Dorking, Surrey, RH5 6NT, U.K.* (cf2@mssl.ucl.ac.uk)

[2] *Instituto de Astronomía y Física del Espacio, IAFE, CC. 67 Suc. 28, 1428 Buenos Aires, Argentina*

[3] *Departamento de Física, Facultad de Ciencias Exactas y Naturales, Universidad de Buenos Aires, Argentina*

[4] *Centre d'Etudes Spatiales des Rayonnements (CESR), CNRS, Toulouse, France*

[5] *Southwest Research Institute, 6220 Culebra Road, San Antonio, TX 78238, U.S.A.*

[6] *Center for Space Physics, Boston University, 725 Commonwealth Avenue, Boston, MA 02215, U.S.A.*

Received November 13, 2006; accepted March 11, 2007

Abstract. We examine the near-Earth Interplanetary Coronal Mass Ejection (ICME) apparently related to the intense Solar Energetic Particle (SEP) event of January 20, 2005. Our purpose is to contribute to the understanding of the macroscopic structure, evolution and dynamics of the solar corona and heliosphere. Using *Cluster*, *ACE* and *Wind* data in the solar wind, and *Geotail* data in the magnetosheath, we perform a multi-spacecraft analysis of the ICME-driven shock, post-shock magnetic discontinuities and ejecta. Traversals by the well-separated near-Earth spacecraft provide a coherent picture of the ICME geometry. Following the shock, the ICME sequence starts with a hot pileup, *i.e.* a sheath, followed by a fast ejecta characterised by a non-compressive density enhancement (NCDE), which is caused essentially by an enrichment in helium. The plasma and magnetic observations of the ejecta are consistent with the outskirts of a structure in strong expansion, consisting of nested magnetic loops still connected to the Sun. Within the leading edge of the ejecta, we establish the presence of a tilted current sheet substructure. An analysis of the observations suggests that the tilted current sheet is draped within the overlying cloud canopy, ahead of a magnetic cloud-like structure. The flux rope interpretation of this structure near L1, confirmed by observations of the corresponding magnetic cloud, provided by *Ulysses* at 5.3 AU and away from the Sun-Earth line, indicate that the bulk of the cloud is in the north-west sector as seen from the Earth, with its axis nearly perpendicular to the ecliptic. This is consistent with the primary direction of travel of the fast halo-CME observed at the Sun. Moreover, the NCDE and helium enrichment are consistent with the position near the streamer belt of the flaring active region NOAA 10720 associated with the CME. However, differences between interplanetary and solar observations indicate a large rotation of the erupting filament and overlying arcade, which can be attributed to the flux rope being subject to the helical kink instability.

1. Introduction

Interplanetary Coronal Mass Ejections (ICMEs) are transient structures in the ambient solar wind. They move away from the Sun into the interplanetary medium with (supersonic) speeds that may be slower (*e.g.*, Tsurutani et al., 2004) or faster (*e.g.*, Lepping et al., 2001) than the ambient solar wind speed. The solar ejecta compresses and deflects the upstream flow, and, for fast ICMEs, a fast shock forms ahead of the ejecta. In magnetic clouds (MCs), representing a subset of ICMEs, the ejecta is interpreted as being contained within a magnetic flux rope (*e.g.*, Burlaga et al., 1981). However, the 3D structure and extent of this flux-rope is generally not known. The compressed region of solar wind behind the shock, the sheath, is draped around the leading edge of the ICME, which is thought to lead to the formation of planar magnetic structures consisting of ordered sheets of magnetic fields (Farrugia et al., 1990; Neugebauer, Clay and Gosling, 1993).

The magnetic field and plasma properties of ICMEs can differ significantly from that of the ambient solar wind. Some of those properties are known to control the interaction of ICMEs with the Earth's magnetosphere. Specifically, through extended periods of strong southward magnetic field and increased solar wind flow speed, ICMEs are often associated with the factors leading to magnetic reconnection at the dayside magnetopause and the resulting geomagnetic activity (*e.g.*, Gonzalez and Tsurutani, 1987). In this respect, not only ejecta, but also ICME sheaths are important to understand such interactions (*e.g.*, Owens et al., 2005; Huttunen et al., 2005), *i.e.* the strong southward magnetic fields may be due to the internal fields of the ejecta or to the compressed fields in the sheath. Consequently, the solar origins and interplanetary evolution of ICMEs represent key research topics relevant to space weather near the Earth (see Schwenn, 2006, for a recent review). Of particular interest are the MCs, which give evidence of flux rope topologies and which may then be connected to their solar counterparts.

The heliolongitude of the source region and principal axis orientation of ICMEs (corresponding to the flux rope axis orientation for MCs), are key aspects to understand the ICME 3D-structure, extent into interplanetary space and its likely effect on the Earth's magnetosphere. Multi-event statistical studies suggest that ICMEs may extend up to $\sim 50^\circ$ in longitude west and east of the solar event location (*e.g.*, Borrini et al., 1982; Cane and Richardson, 2003). In contrast, using multiple spacecraft that are widely separated in the heliosphere, studies of individual ICMEs indicate smaller longitudinal extents, up to $\sim 60^\circ$ in total (Bothmer and Schwenn, 1998).

A reasonably good correspondence between the tilts of filaments (or neutral lines) relative to the solar equator and the orientations of associated MC axis relative to the ecliptic plane has been demonstrated for some events (*e.g.*, Zhao and Hoeksema, 1997; Webb et al., 2000; Fazakerley et al.,

2005). However, more recently, a few cases showing large differences have been reported (Rust et al., 2005; Wang et al., 2006). Meanwhile, more and more evidence for filament eruptions with axial rotation in the solar corona, presumably resulting from the kink instability, has been reported (Rust, 2003; Rust and LaBonte, 2005; Williams et al., 2005; Zhou et al., 2006). Therefore the identification of solar sources of ICMEs, in particular those that involved filament eruptions (*e.g.*, Cremades and Bothmer, 2004), is helpful to the understanding of the coronal mass ejection (CME) onset and evolution in the corona and heliosphere.

The MC terminology is an operational definition (Burlaga, 2001) introduced to identify a feature satisfying three plasma and magnetic field characteristics: (a) a strongly enhanced magnetic field intensity (with respect to ambient values), (b) a low proton temperature and (c) a smooth and large coherent rotation of the magnetic field vector (*e.g.*, Burlaga et al., 1981; Burlaga et al., 2001). The global magnetic structure of a MC ejecta is believed to be a twisted magnetic flux tube (Marubashi, 1986; Bothmer and Schwenn, 1998), whose large-scale topology may be estimated by fitting models to the magnetic field time series (*e.g.*, Lepping, Burlaga and Jones, 1990; Bothmer and Schwenn, 1998; Hu and Sonnerup, 2001; Dasso et al., 2005).

For other (non-cloud) ICMEs, the large-scale topology is more difficult to estimate. The orientation of the draped, compressed fields in the sheath may be used to infer the ejecta axis of non-cloud fast ICMEs (Jones et al., 2002). However, this method assumes that the normal of each discontinuity in the planar structure is aligned with the normal of the ejecta's leading edge, which itself is assumed to be perpendicular to the ejecta axis, consistent with the ejecta driving the shock. Such agreement between the shock normal and the direction perpendicular to the ejecta axis is found in observations of fast MCs (with ramming speeds larger than 600 $\mathrm{km\,s^{-1}}$) (Lepping et al., 2001; Szabo et al., 2001). Shocks driven by fast clouds remain more planar than those driven by slower clouds (ramming speeds less than 400 $\mathrm{km\,s^{-1}}$), whose normals flare away from the cloud's central axis towards the flanks (Szabo et al., 2001).

Nonetheless, it is possible to identify magnetic cloud-like structures (MCLs) (Lepping, Wu and Berdichevsky, 2005) using the classic definition of a MC, except that a flux rope model cannot be fitted. In doing so, Wu, Lepping and Gopalswamy (2006) found that the occurrence rate of MCLs and joint sets (MCs plus MCLs) are related to both the solar activity and the CME occurrence rate, a correlation which could not be found with MCs alone (Wu, Lepping and Gopalswamy, 2003; Huttunen et al., 2005). A MC is usually identified and reported when a spacecraft passes near its cloud axis. It is possible that all ICMEs contain flux ropes, but that some are not recognised as MCs only because the spacecraft trajectories skim the flanks

(Marubashi, 1997). MCLs fitted to torus-shaped flux ropes by Marubashi (1997) were interpreted as curved portions of flux rope structures. Yet, the connections between MCs and MCLs remain to be determined.

The Solar Energetic Particle (SEP) event of January 20, 2005 has been studied extensively in order to understand the mechanisms controlling its exceptional characteristics, such as the rapid arrival of the high energy particles, their intensity and hard energy spectra and the high speed of the associated coronal mass ejection (*e.g.*, Mewaldt et al., 2005; Gopalswamy et al., 2005; Simnett, 2006; Tylka, 2006). Here, we examine the apparently related ICME observed near Earth. Our objective is to contribute to the understanding of the macroscopic structure, evolution and dynamics of the solar corona and heliosphere (see, *e.g.*, Mandrini et al., 2005; Fazakerley et al., 2005; Crooker and Webb, 2006). With the advent of *Cluster*, the analysis of multi-spacecraft observations in the near-Earth solar wind can provide a more elaborate picture of ICMEs (in particular some of their 3D substructure, which may be used to infer properties at larger scales) and of their possible forms of interaction with the Earth's magnetosphere. Using *Cluster*, the Advanced Composition Explorer (*ACE*) and *Wind* data in the solar wind, and to a lesser extent *Geotail* data in the magnetosheath, we perform a multi-spacecraft analysis at one Astronomical Unit (AU) of the ICME-driven shock, post-shock magnetic discontinuities and ejecta. After a preliminary overview of the observations and the identification of the ICME boundaries in Section 2, we analyse the leading magnetic discontinuities in Section 3 and discuss the possible geometry of the ejecta modeled as a flux rope in Section 4. In Section 5, we confirm our interpretation of the ejecta, a MCL, with observations of the corresponding MC provided by *Ulysses* away from the Sun-Earth line. In Section 6, we summarise and interpret the global geometry of the ICME, and, through comparison with the corresponding solar observations, discuss its likely formation and evolution in the corona and heliosphere.

2. Overview of near-Earth multi-spacecraft observations and identification of boundaries

2.1. Spacecraft distribution in near-Earth space

In this work, we use the Geocentric Solar Ecliptic (GSE) system of reference ($\hat{\mathbf{X}}_{GSE}$, $\hat{\mathbf{Y}}_{GSE}$, $\hat{\mathbf{Z}}_{GSE}$). In this coordinate system, $\hat{\mathbf{X}}_{GSE}$ points from the Earth toward the Sun, $\hat{\mathbf{Y}}_{GSE}$ is in the ecliptic plane pointing toward dusk when an observer is near Earth (opposing planetary motion) and thus $\hat{\mathbf{Z}}_{GSE}$ is parallel to the ecliptic pole and points to the north. We also define sectors in the plane of the sky, relative to the Sun, as seen from the Earth. East and west sectors correspond to dusk and dawn sectors respectively.

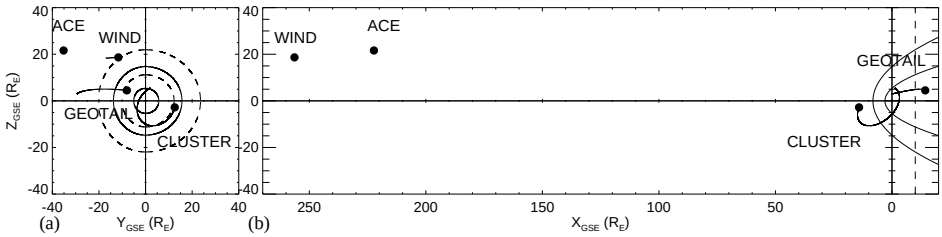

Figure 1. Spacecraft positions and orbit traces, in the GSE Cartesian coordinate system, during the passage of the ICME on January 21-22, 2005 in (left) the plane across the Sun-Earth line (as seen from the Sun) and (right) the noon-midnight meridional plane. The spacecraft positions on January 21, 2005 at 12 UT are shown as full circles. Orbit traces are shown from those starting positions until January 22, 2005 at 24 UT. A solar wind pressure of 50 nPa and an IMF B_z of 0 nT were used to compute the GSE aberrated magnetopause model from Roelof and Sibeck (1993) and bow shock model from Fairfield (1971). In panel (a) they are represented by plain contours at $X_{GSE} = 0$ R_E and dashed contours at $X_{GSE} = -10$ R_E. The level $X_{GSE} = -10$ R_E is also indicated as a dashed line in panel (b).

The ICME event affecting near-Earth space on January 21, 2005 starts with a shock arrival at around 16:47 UT near the L1 Lagrangian point upstream to the Earth. *Wind* and *ACE* are located at these upstream distances with *Wind* 13-R_E and *ACE* 35-R_E dawnward of the Sun-Earth line. *ACE* is the furthest north, at Z_{GSE}=22 R_E , 4 R_E northward of *Wind*. *Cluster* and *Geotail* are nearer the Earth, *Cluster* on the duskside and *Geotail* on the dawnside. See Figure 1. During the passage of the ICME, *Cluster* samples the solar wind upstream of the bow shock. *Geotail* is on an outbound section of its orbit, moving from the magnetosphere into the magnetosheath, and possibly sampling the solar wind. As it moves outward, *Geotail* reaches positions further dawnward than *Wind* (by 3 R_E at 20 UT and by 6 R_E at 24 UT on January 21) .

2.2. The leading edge of the ICME

Figure 2 gives an overview of the leading edge of the ICME. This includes magnetic and plasma in-situ observations, provided by the instruments listed in Table 1. Plasma measurements from *ACE* and *Geotail* are displayed for protons. *Cluster-3* profiles are for ions. In the case of *Cluster-3*, the temperature shown is the component perpendicular to the magnetic field, which shows much less scatter than the field-aligned components. Ion measurements (bulk speed, temperature and density) were not available from the Solar Wind Experiment (SWE) (Ogilvie et al., 1995) on *Wind*. The time series for each dataset are synchronised with the ICME shock arrival at *ACE*, denoted SA: *Wind*, *Cluster-3* and *Geotail* time series are shifted by

Table 1. Instruments providing magnetic field and plasma in-situ measurements near Earth.

Mission	Magnetic field	Plasma
Wind	Magnetic Field Investigation (MFI) (Lepping et al., 1995)	Not used
ACE	Magnetic Fields Experiment (MAG) (Smith et al., 1998)	Solar Wind Electron Proton Alpha Monitor (SWEPAM) (McComas et al., 1998)
Cluster	Flux Gate Magnetometer (FGM) (Balogh et al., 2001) - used on C3	*Cluster* Ion Spectrometry (CIS) experiment (Rème et al., 2001) - Hot Ion Analyser (HIA) used on C3 and Composition and Distribution Function analyser (CODIF) used on C4
Geotail	Magnetic Field investigation (MGF) (Kokubun et al., 1994)	Solar Wind Analyser (SWA) from the comprehensive plasma instrument (CPI) (Frank et al., 1994)

233s, −1380s and −1567s respectively (so that the shock arrival recorded at each position is aligned with the shock passage at *ACE*).

The upstream solar wind conditions are illustrated with the observations from *Wind* and *ACE* (shown in black and red respectively). *Cluster* (green) is also in the solar wind during the whole time interval shown. Simultaneously with the extrapolated time for the passage of the shock, SA, *Geotail* (blue) crosses the magnetopause, moving outbound from the magnetosphere into the magnetosheath (evidenced by the jump in density in Figure 2e). The magnetosheath observations are, as expected, offset with respect to the values found in the solar wind. They are characterised in Figure 2 by higher values in magnetic field, $B(=|\mathbf{B}|)$, density, N, and temperature, T, and lower values in bulk flow speed, $V(=|\mathbf{V}|)$.

The arrival of the shock SA is followed by a secondary front or post-shock discontinuity, SB (around 18:20 UT at *ACE*). The arrival of SB is well synchronised between the four missions. The temperature and density plots of Figure 2d,e reveal two distinct thermal structures of the ICME: first, from SA, a hot pileup consistent with a sheath, followed, from SB, by a colder, denser pileup, consistent with a non-compressive density enhancement (NCDE) (Gosling et al., 1977). The NCDE characteristics are

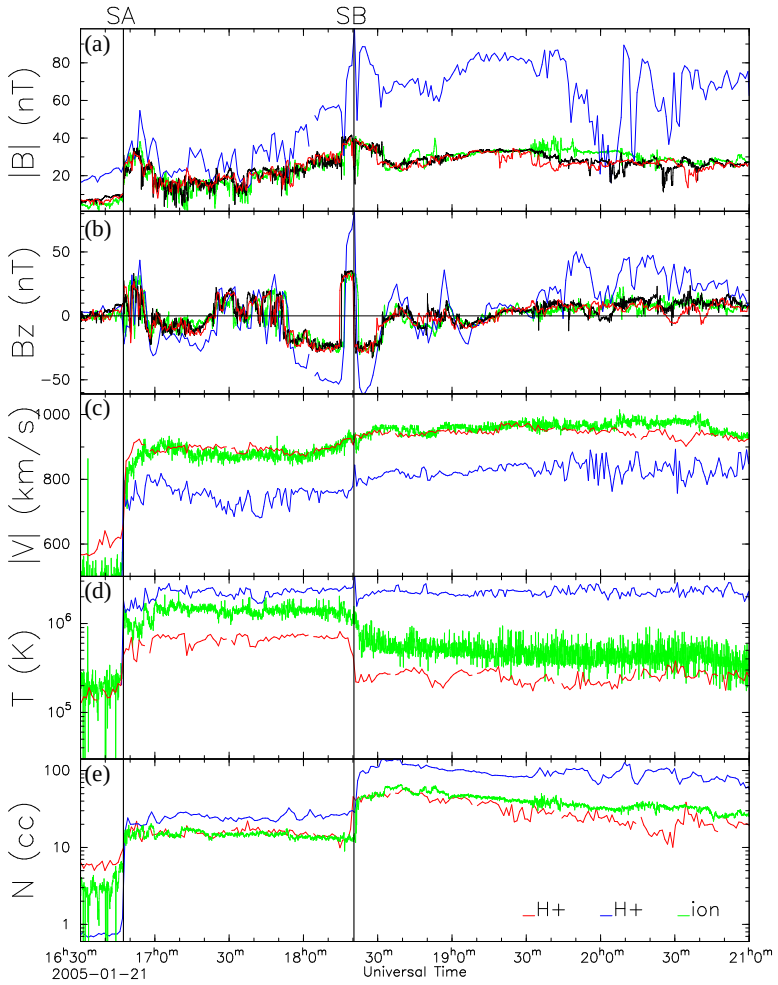

Figure 2. The leading edge of the ICME observed on January 21, 2005 by *Wind* (black), *ACE* (red), *Cluster-3* (green) and *Geotail* (blue). The plot shows (a) the total and (b) the north-south component of the magnetic field, (c) the plasma bulk flow speed, (d) temperature and (e) number density (ion or proton depending on the mission). The time series are synchronised with the ICME shock arrival at *ACE*. Vertical lines indicate the arrival of the shock, SA, and a secondary front, SB. SA corresponds also to the passage of *Geotail* from the magnetosphere to the magnetosheath.

its large proton densities (peaking above 15 cm^{-3} and measured when the bulk flow speed is nearly constant) and the property of the temperature to vary inversely as the density during the NCDE.

The sheath is also characterised by magnetic fluctuations, an increase in magnetic field strength and a jump in wind velocity from 560 to 900 $km\,s^{-1}$ after the ICME shock arrival (see Figure 2a-c). The magnetic field turns strongly southward, with a north-south component reaching about -

30 nT in the back edge of the sheath (Figure 2b). Once these conditions reach Earth, they trigger a Sudden Storm Commencement (SSC) observed at 17:11 UT on January 21 (original time), followed by a geomagnetic storm with a disturbance storm-time (Dst) perturbation of about -100 nT (according to the National Geophysical Data Center (NGDC)). An analysis of the magnetospheric and magnetosheath modifications induced by this event, in particular through the effects observed on the Double Star TC1 satellite, was presented by Vallat et al. (2005).

2.3. Identification of the ejecta boundaries

It is of interest to identify the boundaries of the ejecta and to examine whether it may be classified as a magnetic cloud (MC). The identification of the MC boundaries cannot be determined for some clouds, mainly because different proxies can provide different positions (Russell and Shinde, 2005; Dasso et al., 2006). The boundaries of the observed fast ejecta that we propose, its first encounter coinciding with SB followed by the boundaries, CA and CB, of a possible magnetic cloud-like structure (MCL), are indicated in Figure 3 with vertical annotated lines. Several proxies indicate that these observations are consistent with the observation of an ICME and, more specifically, a MCL, *i.e.* showing the same fatures as a MC, except for the large coherent rotation of the magnetic field (Figure 3b,c).

Firstly, for the same bulk flow speed, the proton temperature, T_p, in ejecta is considerably lower than in the solar wind (see, *e.g.*, Gosling, 1990; Richardson and Cane, 1995 and references therein). Systematic identifications of ejecta have been done (see, *e.g.*, Cane and Richardson, 2003) from point by point comparison of the observed proton temperature, T_p, with the expected temperature, T_{ex}, appropriate for normally expanding solar wind. T_{ex} is essentially the typical temperature found in the ambient solar wind, with observed speed V_{sw}, and is inferred using an empirical correlation between the proton temperature and the solar wind speed. Based on 3 years of measurements from *ACE*/SWEPAM, this relation takes the form (Neugebauer et al., 2003)

$$T_{ex} = \begin{cases} -0.1337 V_{sw}^2 + 487.8 V_{sw} - 110788.3, & V_{sw} < 450\,\mathrm{km\,s^{-1}} \\ -0.4295 V_{sw}^2 + 1002.5 V_{sw} - 272732.3, & V_{sw} \geq 450\,\mathrm{km\,s^{-1}} \end{cases},$$

where V_{sw} is in $\mathrm{km\,s^{-1}}$and T_{ex} in K.

Figure 3e shows the observed (radial) proton temperature T_p from *ACE* (black line), the expected temperature T_{ex} (plain red line) computed from the observed solar wind speed (shown in Figure 3d) and $T_{ex}/2$ (dashed red line). Richardson and Cane (1995) found that $T_p < T_{ex}/2$ can be considered as one of the criteria to identify ICMEs in the interplanetary medium. A large part of the interval proposed for the ejecta, in particular the last two

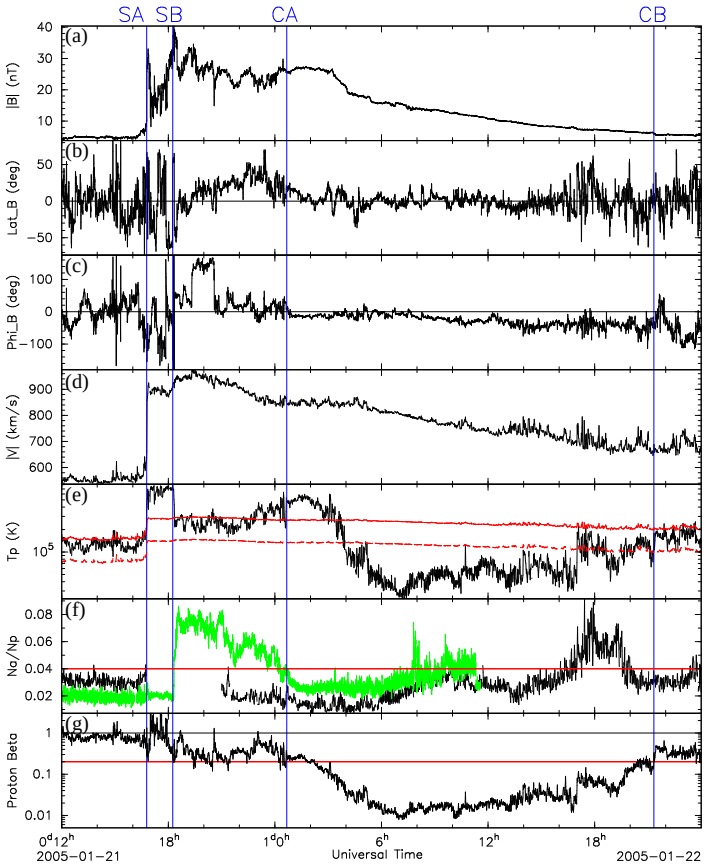

Figure 3. The ICME observed on January 21-22, 2005 by *ACE*, supplemented by data from *Cluster-4*. The plot shows (a) the total, (b) the elevation and (c) azimuthal (mod π) components of the magnetic field, (d) the plasma (proton) bulk flow speed, (e) the proton temperature (black), the expected temperature T_{ex} (plain red line) computed from the observed solar wind speed and $T_{ex}/2$ (dashed red line), (f) the alpha to proton density ratio from *ACE* (black) and *Cluster-4* (green, time-shifted), the typical 4% ratio observed in the solar wind (red) and (g) the proton plasma beta (black) and a threshold of 0.2 (red). Vertical lines indicate the arrival of the shock, SA, the ejecta front, SB, and the boundaries, CA and CB, of a possible MCL.

thirds of the interval, corresponds to a region where $T_p < T_{ex}/2$, consistent with the passage of an ICME.

Secondly, the α-particle to proton density ratio is highly variable inside a given ejecta, and may differ markedly from the typical 4% ratio observed in the solar wind, reaching lower values and also values as high as $\sim$ 20% (Borrini et al., 1982; Galvin et al., 1987). Figure 3f shows that the ratio obtained with *ACE* (black line) reaches a minimum of $\sim$ 1% and a maximum of $\sim$ 8% in the interval proposed for the ejecta. However, the leading edge of the ICME and the proposed ejecta front boundary are within a data gap in

this ratio from *ACE*. This gap is supplemented by the corresponding ratio obtained with *Cluster-4*/CIS/CODIF (green line in Figure 3f; the *Cluster* time-series are shifted by -1567s, so that the shock passage at *Cluster* aligns with the shock passage at *ACE*). This ratio is given until *Cluster* moves into the magnetosphere. The alpha particle measurements by CODIF are limited by proton pollution and detector saturation in the solar wind. Therefore, the ratio shown has been scaled down by a factor of 5 in order to agree, within the same order of magnitude, with the *ACE* ratio. In this instance, the diagnostic supplemented by *Cluster* is helpful to identify the ejecta front boundary, which coincides with the start of the NCDE (front SB). The analysis of the composition in protons and alpha particles provided by CODIF shows that the NCDE is caused essentially by an enrichment in helium. The possibility that this helium enhancement lies outside the ICME boundaries (Neugebauer and Goldstein, 1997) seems unlikely owing to the simultaneous drop in temperature. The coincident onset of the helium enhancement and the leading edge of a temperature depression has been previously observed (Bame et al., 1979). The second enhancement near 18 UT on January 22, towards the trailing part of the ejecta, is consistent with statistical studies by Richardson and Cane (2004a), who found that the occurrence rate of helium enhancements (above the 6% ratio) increase towards the trailing part of ICMEs or MCs. Their study also shows that, statistically, MCs are more likely to show the helium enhancements than non-cloud ICMEs.

Finally, MCs are identified by their low values in plasma β. Inside the proposed time range, the proton plasma beta, β_p, is mostly below 0.5 (Figure 3g). Correspondingly, low levels of magnetic fluctuations are observed, for instance in the magnetic field elevation angle (Figure 3b). Such low plasma β signatures are found elsewhere in parcels of interplanetary fluid (Mullan et al., 2003; Mullan and Smith, 2006). From a statistical study of 19 magnetic clouds at 1 AU, Lepping et al. (2003) found that inside the average cloud $\beta_p = 0.12 \pm 0.06$. Hence MCs may be identified as regions with values of β_p below an acceptable threshold of 0.2. The drops in field-magnitude fluctuations and β_p, around 00:40 UT on January 22, strongly suggest that the spacecraft entered a MCL at this time (CA). We consider the sharp increase in plasma β_p around 21:20 UT on January 22 (coincident with $T_p \sim T_{ex}$ in Figure 3e) to mark the ejecta trailing boundary (CB). Therefore the embedded MCL, between CA and CB, is about 75% the size of the ICME. In Section 4, we will examine the geometry of the ejecta in more detail.

In the following section, we first discuss the driven shock and magnetic discontinuities found in the leading edge of the ICME, namely the sheath and then the leading edge of the ejecta.

3. The leading magnetic discontinuities: global geometry and substructure

3.1. Observations

Figure 4 gives a closer look at the leading edge of the ICME, with a different view on aspects of plasma and magnetic observations than in Figure 2. Across the shock SA, the solar wind dynamic pressure increases from 5 to 20 nPa (Figure 4a). The secondary front SB, which we identified as the leading boundary of the ejecta, forms behind a magnetic discontinuity. As shown in Figure 4b-d, the IMF points mainly inward (*i.e.* towards the Sun, $B_x > 0$) and southward ($B_z < 0$), before and after the passage of the ejecta front layer. In the front layer itself, between SB1 and SB2, the magnetic field points almost in the opposite direction ($B_x < 0$ and $B_z > 0$), while the dusk-dawn component (B_y) turns smoothly from west to east (*i.e.* B_y from negative to positive). Across SB2, the solar wind dynamic pressure increases from 20 to more than 60 nPa (Figure 4a).

In the leading edge of the ejecta, following the front SB, variations in density lead initially to the further increase of the solar wind dynamic pressure. It is worth noting that, in the period rich in helium, between SB and CA, alpha particles are taken for protons by CIS/HIA and probably by *ACE*/SWEPAM, so that the solar wind dynamic pressure from *Cluster* ion and *ACE* proton measurements might be slightly overestimated. For a plasma containing $\sim 8\%$ of alpha particles, the partial pressure is overestimated by $\sqrt{2}$. Hence the peak in dynamic pressure at 90 nPa is more likely to represent a real value of 63 nPa, closer to the plasma pressure measurement from *Geotail*. Over the remainder of the interval shown, this decreases back to 30 nPa (Figure 4a). The IMF, which is initially pointing southward ($B_z < 0$), progressively turns into the ecliptic plane and further slightly northward ($B_z > 0$) (Figure 4d). Its direction with respect to the Sun is still mainly inward ($B_x > 0$) (Figure 4b). Departures from these initial synchronised conditions then occur, which differ in space between the four missions, located upstream and around the Earth.

In the dawn sector, *ACE*, *Wind* and *Geotail* observe a magnetic layer discontinuity, across which the IMF component along the Sun-Earth line reverses its sign. This discontinuity is not observed by *Cluster* in the dusk sector (Figure 4b). *ACE* is first to cross the discontinuity (marked by a vertical line denoted SC1), moving into a region of outward IMF ($B_x < 0$), and is last to cross it back (at SC2). *Wind* samples the region for a shorter time: the in-and-out discontinuity crossings at *Wind* are nested between the corresponding crossings at *ACE*. *Geotail* passes three times through the region of outward IMF (in the magnetosheath): this happens, during the first two passages, when *Wind* and *ACE* are also on that side of the

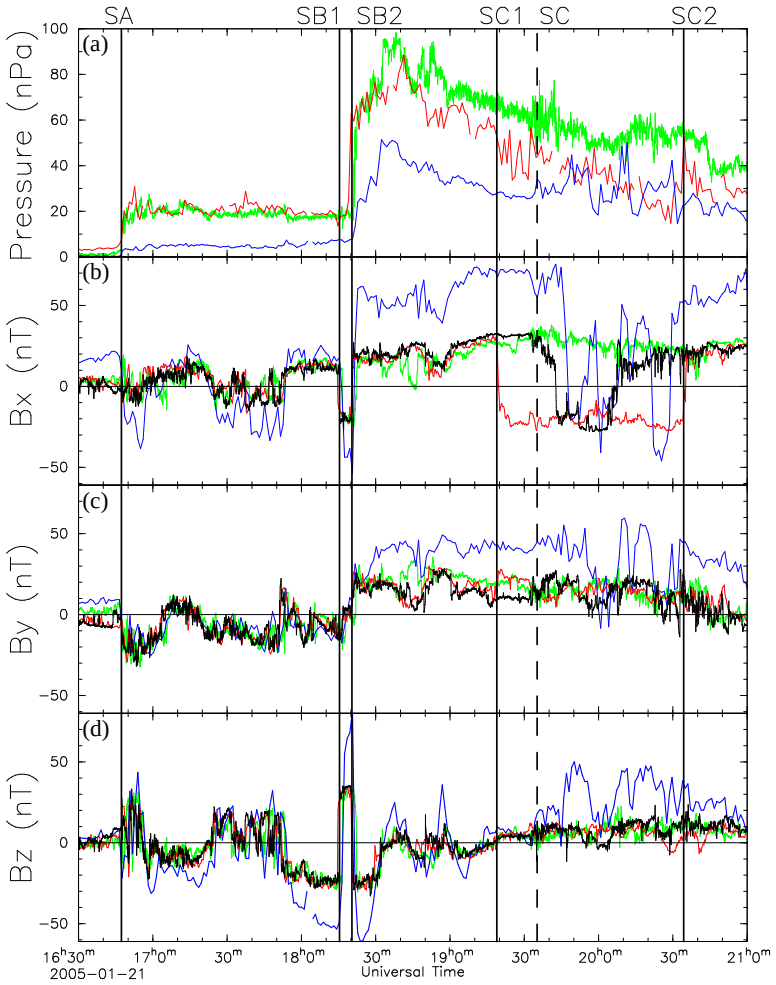

Figure 4. ICME leading edge observed on January 21, 2005 by *Wind* (black), *ACE* (red), *Cluster-3* (green) and *Geotail* (blue). The plot shows (a) the solar wind dynamic pressure observed at *ACE* and *Cluster-3*, and the plasma pressure from the CPI/HPA (0.05-50 keV) instrument on *Geotail*, (b-d) the magnetic field components (in GSE Cartesian coordinates). As in Figure 2, the time series are synchronised with the ICME shock arrival at *ACE*. Vertical lines indicate the arrival of the shock SA, front discontinuities SB1 and SB2, pair SC1 and SC2 of in-and-out magnetic discontinuity crossings at *ACE* and, shown as a dashed line, a reference time within the region of outward IMF, SC.

discontinuity; the last and third passage occurs when *Wind* is back into the inward IMF region and *ACE* is still in the outward IMF region. Those passages of *Geotail* through the region of outward IMF are associated with variations in plasma pressure in the magnetosheath. Variations of similar amplitudes in solar wind dynamic pressure are not observed near L1 at *ACE* in the corresponding region (Figure 4a).

Table 2. Results of 4-spacecraft timing analysis, single-spacecraft MVA and cross-product analysis for the driven shock and magnetic discontinuities in the leading edge of the ICME of January 21, 2005. The table lists, from left to right, the crossing time (time-shifted to the *ACE* time frame), the discontinuity name, the analysis technique and the spacecraft concerned, the obtained normal vector **N** in GSE Cartesian coordinates, the net velocity V_N ($\mathrm{km\,s^{-1}}$) along it, the angle θ_{BN} (°) between the upstream magnetic field and **N**.

Time	Dis.	Analysis - S/C	**N** (GSE)	V_N	θ_{BN}
16:47:19	SA	4-sc *Cluster*	(-0.974, -0.092, 0.207)	930	100.7
18:15:23	SB1	4-sc *Cluster*	(-0.810, 0.080, -0.581)	798	88.5
		MVA C3	(-0.868, 0.083, -0.489)		
		MVA *ACE*	(-0.866, -0.194, -0.460)		83.3
		MVA *Wind*	(-0.838, 0.062, -0.542)		
18:20:23	SB2	4-sc *Cluster*	(-0.851, -0.011, -0.525)	837	78.3
		MVA C3	(-0.872, 0.289, -0.395)		
		MVA *ACE*	(-0.838, 0.062, -0.542)		87.6
		MVA *Wind*	(-0.750, -0.315, -0.582)		
19:18:53	SC1	MVA *ACE*	(0.146, -0.046, 0.988)		86.2
		Crossed-B *ACE*	(0.161, -0.345, 0.925)		
19:35:37	SC1	MVA *Wind*	(0.014, -0.395, 0.918)		85.5
		Crossed-B *Wind*	(0.161, -0.189, 0.967)		
19:58:37	SC2	MVA *Wind*	(-0.189, -0.380, 0.905)		77.4
		Crossed-B *Wind*	(-0.444, -0.101, 0.890)		
20:34:23	SC2	MVA *ACE*	(-0.167, -0.325, 0.931)		95.1
		Crossed-B *ACE*	(-0.106, -0.420, 0.901)		

While the ICME is a large-scale phenomenon observed by all spacecraft, the differences between the spacecraft indicate the presence of a substructure. We next examine the exact geometries and timings of the events observed in order to determine the global geometry and substructure of the ICME leading edge.

3.2. Multi-spacecraft analysis

We determine the characteristics of the driven shock and magnetic discontinuities identified in the ICME leading edge, using the magnetic field and plasma measurements. For each discontinuity observed by *Cluster*, we perform a 4-spacecraft timing analysis on the magnetic field data, which

provides estimates of the surface normal vector **N** and velocity V_N (Schwartz, 1998). This method assumes a locally planar front passing over the 4 *Cluster* spacecraft, which are arranged at this time in a near tetrahedral configuration, roughly 600 km apart. Minimum Variance Analysis (MVA) is also used on single-spacecraft magnetic field data to infer normal vectors (when a well defined set of eigenvectors is returned; see, *e.g.*, Sonnerup and Scheible, 1998). The cross-product of the magnetic field vectors across the discontinuities SC1 and SC2 (not observed by *Cluster*) is used to infer magnetic coplanarity normals (Schwartz, 1998). In addition, we determine the angle θ_{BN} between the upstream magnetic field and **N**. The results are shown in Table 2. There is generally a good agreement between discontinuity orientations derived from the MVA technique on single spacecraft and those obtained from multi-spacecraft timing. The orientations derived from the cross-product analysis also confirm the MVA results in the case of the discontinuities SC1 and SC2.

The magnetic fields upstream of the shock and discontinuities are all almost perpendicular with respect to the normals. The normal direction at SA, in this case a quasi-perpendicular shock, points slightly westwards and northwards. The shock speed, along the normal and relative to the upstream solar wind, is 374 $\mathrm{km\,s^{-1}}$. The upstream Alfvén Mach number $M_A = 5.9$ and plasma $\beta = 1.7$. These parameters are derived from the magnetic field, proton bulk flow velocity, temperature and number density measured immediately upstream of the shocks or discontinuities, by assuming an electron-proton plasma. We also found that the post-shock discontinuities in the sheath have normals parallel to the normal of the shock SA. This is consistent with the draping of heliospheric magnetic fields about fast ICMEs and the formation of planar magnetic structures consisting of ordered sheets of magnetic fields (Gosling and McComas, 1987; McComas et al., 1988; Farrugia et al., 1990; Neugebauer, Clay and Gosling, 1993). Likewise, the normal directions at SB1 and SB2 are aligned with each other. In contrast to the normal direction at SA, they point along the Sun-Earth line and slightly southwards. The size of the ejecta front layer SB1-SB2 is 38.4 $\mathrm{R_E}$ based on the average speed along the average front normal (obtained from 4-spacecraft timing analysis at SB1 and SB2).

The speeds of the ejecta front (SB1-SB2), determined by 4-spacecraft timing at *Cluster*, are about 100 $\mathrm{km\,s^{-1}}$lower than the net shock velocity of 930 $\mathrm{km\,s^{-1}}$ (905 $\mathrm{km\,s^{-1}}$ along the Sun-Earth line). Between the Sun and L1, the average 'transit' speed of the ICME region is $\sim$ 1200 $\mathrm{km\,s^{-1}}$, if one assumes that the SA shock corresponds to the arrival at 1 AU, after 34 hours, of the shock driven by the halo CME of January 20 (departing around 6 UT from the Sun). As expected for a shock and for a fast ejecta front, which slow down as they travel through interplanetary space (see, *e.g.*, Forbes et al., 2006; Forsyth et al., 2006, for recent reviews), this average value is found

to be intermediate between the speed estimates in the corona, which range from 2500 to 3700 $\mathrm{km\,s^{-1}}$ (Gopalswamy et al., 2005; Tylka, 2006), and the net shock and ejecta front velocities. Connections to the Sun are further discussed in Section 6.

The normals of discontinuities SC1 and SC2, determined at *ACE* and at *Wind*, are principally orientated in the north-south direction. Figure 5 represents those normals projected in the noon-midnight meridional and ecliptic planes. The normals are positioned at a fixed common time SC (indicated in Figure 4). For instance, discontinuity crossings SC1 and SC2, occurring respectively before and after the time SC, are shown at extrapolated positions respectively after and before transport in the solar wind. The solar wind speed is taken to be the average of bulk flow speeds at *ACE* measured at crossings SC1 and SC2, *viz.* $\mathbf{V_{sw}} = [-923.7, 35.8, 35.1]$ $\mathrm{km\,s^{-1}}$ in GSE Cartesian coordinates. We find that the size of the outward IMF region, between SC1 and SC2, along the Sun-Earth line is 196 $\mathrm{R_E}$ for *Wind* (at Y_{GSE}= -13 $\mathrm{R_E}$ and Z_{GSE}=18 $\mathrm{R_E}$) and 657 $\mathrm{R_E}$ for *ACE* (at Y_{GSE}=-35 $\mathrm{R_E}$ and Z_{GSE}=22 $\mathrm{R_E}$). The size of the region measured at *ACE* is much larger than the distances between the four missions. Therefore, in order to have a representation of the discontinuities in the context of their interaction with the magnetosphere, their relative positions along the Sun-Earth line in Figure 5 are scaled down by 5, with respect to the distance to the discontinuity SC1 observed at *Wind* (which is the closest to the subsolar bow shock at time SC).

We propose that the discontinuities SC1 and SC2 form a tilted, curved current sheet whose centre of curvature is in the north-west sector. This configuration can account for the respective normal directions at *ACE* and *Wind*, the nested time intervals from *ACE* and *Wind* on the dawn side and the absence of an observation of this discontinuity on the dusk side by *Cluster*. Since *Geotail* is further dawnward than *Wind* by the time the current sheet passes the spacecraft (Figure 5b), the tilted configuration in the ecliptic plane could also explain why the (extrapolated) passages of *Geotail* through the region of outward IMF still occur after *Wind* is back into the inward IMF region. However, the first (extrapolated) traversal of the discontinuity by *Geotail* occurs later than the first traversal by *Wind*, and *Geotail* is much further south than the expected passage of the current sheet (Figure 5a). Although the *Geotail* traversals of the current sheet in the magnetosheath are not fully consistent with the topology of the current sheet in the solar wind, they may be attributed to effects of the interaction of the tilted current sheet with the magnetosphere.

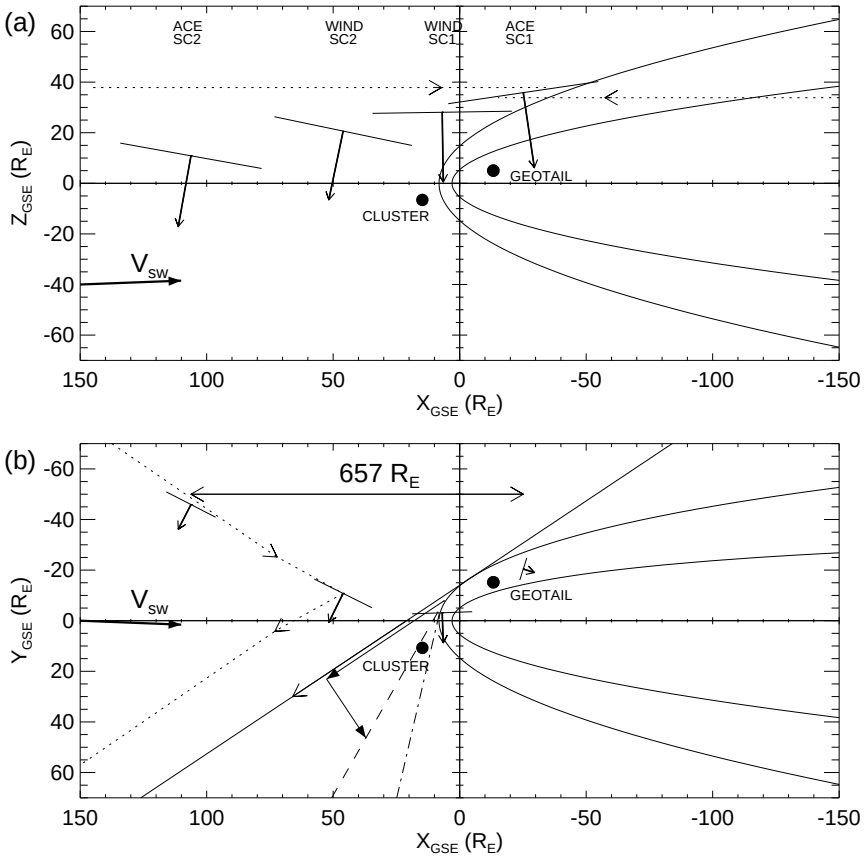

Figure 5. Geometries of a tilted current sheet on the dawn side and the foreshock region on the dusk side. *Geotail* and *Cluster-3* positions are projected onto (a) the noon-midnight meridional plane and (b) the ecliptic plane (in the GSE Cartesian coordinate system). A solar wind pressure of 50 nPa and an IMF B_z of 0 nT were used to compute the GSE aberrated magnetopause model from Roelof and Sibeck (1993) and bow shock model from Fairfield (1971). Pairs of in-and-out discontinuity normals, SC1/SC2, observed at *ACE* and *Wind* are shown (with arbitrary units) at time SC, after/before transport in the solar wind. For clarity, the relative positions along the Sun-Earth line are scaled down by 5, with respect to the distance to the discontinuity SC1 observed at *Wind*. The transitions between inward and outward IMF regions across the tilted current sheet are illustrated with dotted field lines for the crossings SC1 at *ACE* in panel (a) and SC2 at *Wind* in panel (b). The Earth's foreshock region on the dusk side is downstream of the tangent IMF line (shown as a plain line, pointing inward) that first touches the Earth's bow shock. A possible ion foreshock boundary (shown as a dashed line) forms where the guiding center motion of backstreaming ions consists of the parallel motion along the IMF and the cross-field drift motion (shown with filled arrows). A possible ULF foreshock boundary is shown as a dot-dashed line.

4. Geometry of the ejecta: the flux rope hypothesis

To analyse further the ejecta and the MCL identified in Section 2.3, we consider the hypothesis that the MCL may be interpreted as a flux rope with the spacecraft passing through its outskirts (*i.e.* its outer shells, as opposed to its centre).

For a flux rope passing a spacecraft, in such a way that the minimum distance (the impact parameter, p) between the (rectilinear) trajectory of the spacecraft and the flux rope axis is much lower than the flux rope typical size (*e.g.*, its radius R), then a large and coherent rotation of the magnetic field vector is expected during the time of the interplanetary flux rope observation. For observations of a MC modeled as a flux rope with small values of p/R, it is possible to get estimates of the main axis orientation of the flux rope from the observed magnetic field time series, using different techniques (*e.g.*, Lepping, Burlaga and Jones, 1990; Bothmer and Schwenn, 1998; Hu and Sonnerup, 2001; Dasso et al., 2005).

However, for values of p/R larger than ~ 0.7 (*i.e.*, the spacecraft path is near the flux rope periphery), the uncertainties associated with the orientation angles turn out to be very large (Gulisano et al., 2005), and accordingly the large and coherent rotation cannot be easily distinguished. Several observed features indicate that this latter is the case here and, in particular, are consistent with the observation of the outskirts of a strongly expanding flux rope (*i.e.* $0.7 < p/R < 1$).

Firstly, the observations of plasma velocity and magnetic field intensity are consistent with the ejecta being in strong expansion. Velocities starting at $\sim$ 1000 km s^{-1} decrease continuously to reach values of $\sim$ 700 km s^{-1} toward the ejecta trailing boundary (Figure 3d). Due to magnetic flux conservation, it is expected that strongly expanding parcels of magnetised fluid show at the same time strong decrease in B. Figure 3a shows a strong decrease in B, between CA and CB, that is consistent with an expansion.

In the hypothesis of a strongly expanding flux rope (*i.e.*, strong decrease of B), we perform an analysis of the direction of the magnetic field vector using the normalised Cartesian GSE components (using *ACE* data, see Figure 6a-c). As noted previously, the level of fluctuations in the components of the magnetic field are significantly lower inside the MCL. B_z is much lower than B most of the time and tends to be positive; B_x remains near B, while B_y goes from positive to negative (between SB and CB). In general, the magnetic field vector near the periphery of a flux rope has almost no axial field component and is mainly azimuthal, with the field lines rounding its axis (see, *e.g.*, Burlaga et al., 1981). For a rope axis nearly parallel to $\hat{\mathbf{Z}}_{GSE}$, the azimuthal components would be associated with B_x and B_y. We note that the change of sign in B_y is observed to occur before the middle of the ejecta passage time, as expected for a flux rope in radial expansion

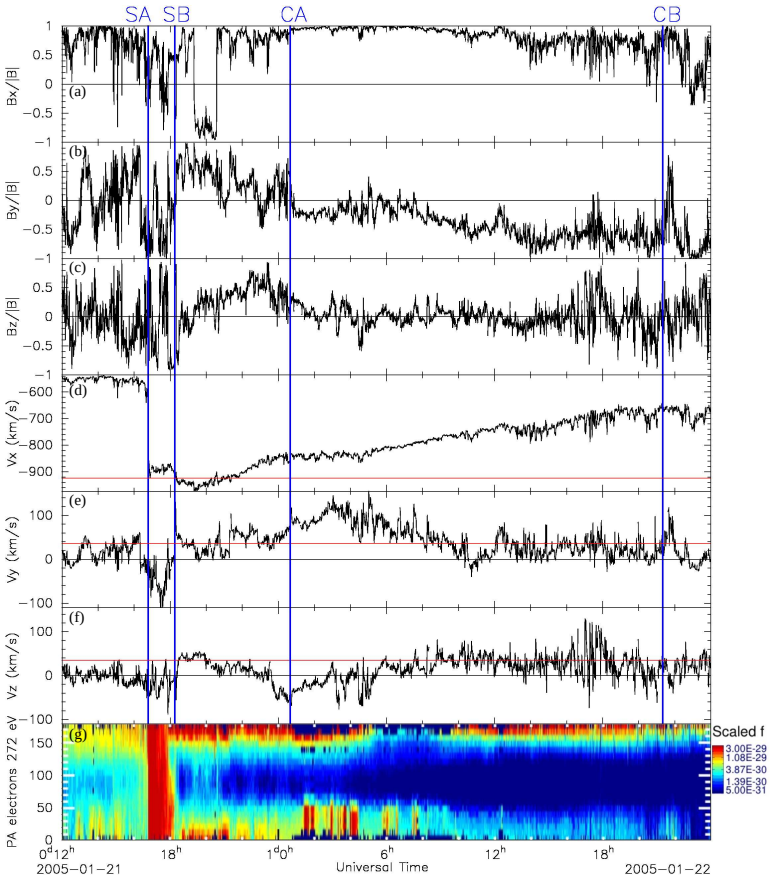

Figure 6. The ICME observed on January 21-22, 2005 by *ACE* (black). The first 6 panels show the normalised components of the magnetic field and the components of the flow vector in the GSE coordinate system. Note that V_x is shown on a different scale than V_y and V_z. Red horizontal lines indicate an average flow speed in the leading edge of the ejecta. The last panel shows the colour-coded pitch angle velocity distributions $f(v)$ of 272 eV electrons, in units of s^3cm^{-6} (from *ACE*/SWEPAM/STEA). Vertical lines indicate the arrival of the shock, SA, the ejecta encounter, SB, and the boundaries, CA and CB, of the MCL, as in Figure 3.

along $\hat{\mathbf{X}}_{GSE}$, with its axis perpendicular to the ecliptic plane. Thus, for these observations of a MCL modeled as a flux rope, we propose that *ACE* passes through the outskirts of an expanding flux rope (p/R lower but of the order of one, *i.e.* a large impact parameter), with the bulk of the structure dawnward from the *ACE* position (and thus dawnward from the Sun-Earth line) and with a flux rope axis perpendicular to the ecliptic plane (*i.e.*, axis nearly parallel to $\hat{\mathbf{Z}}_{GSE}$).

Furthermore, the direction of expansion may be deduced from the components of the flow vector. Figure 6e,f shows those components in the GSE

system (from *ACE*). Red horizontal lines indicate, for reference, an average flow speed in the leading edge of the ejecta (measured at crossings by *ACE* of the current sheet substructure), which represents the ramming speed. In this frame of reference, deviations in the components, V_y and V_z, of the flow perpendicular to the Sun-Earth line, are observed between roughly 21 UT on January 21 and 9 UT on January 22. As it travels from the Sun, the plasma of the ejecta is pushed towards the East and South, with relative speeds reaching about 100 $\mathrm{km\,s^{-1}}$ in both perpendicular directions. These deviations may indicate the directions of the ejecta expansion away from the Sun-Earth line. The eastward expansion in the ejecta is of opposite direction to the flow deflection in the sheath (reaching 100 $\mathrm{km\,s^{-1}}$ westward). Such opposite flows are considered to be the consequence of magnetic pressure build-up ahead of the ICME on its western flank as the Parker-spiral IMF is draped around it (Gosling et al., 1987b). In the sheath, increasing (non-radial) flow velocities are expected to be directed perpendicular to the flux rope axis for observations on the flank of the rope (Owens and Cargill, 2004). Accordingly, the present observations, showing a relatively weak component V_z in the sheath, are consistent with the proposed orientation of the flux rope perpendicular to the ecliptic plane.

The length scale of the ejecta, detected for about a day near L1, is estimated to be of the order of 11,860 $\mathrm{R_E}$ (0.5 AU). In this calculation, the passage time of the ejecta is 26.6 hours, and the mean speed along the Sun-Earth line direction is 790 $\mathrm{km\,s^{-1}}$. Similarly, the length scale of the MCL, between boundaries CA and CB, is found to be 0.39 AU. These respective length scales are of similar order as the length scales estimated for fast MCs (with a maximum speed greater than 600 $\mathrm{km\,s^{-1}}$) by Burlaga et al. (2001), who give an average of 0.5 ± 0.12 AU derived from counter-streaming electrons and an average of 0.39 ± 0.08 AU derived from magnetic field signatures. Such length scales are naturally larger than the typical radial cross-section of 0.28 ± 0.095 AU (Lepping, Burlaga and Jones, 1990), which are obtained for MCs with lower average speeds (450 $\mathrm{km\,s^{-1}}$). They are also 3 times much smaller than those of fast complex ejecta (Burlaga et al., 2001).

Finally, counter-streaming suprathermal electrons are observed within the ejecta by *ACE*/SWEPAM/STEA (pitch angle distributions typically at energies of 272 eV), as indicated in Figure 6g. The counter-streaming suprathermal electrons, observed in the first half of the ejecta passage time, may be interpreted as signatures of nested magnetic loops overlying the flux rope and being still connected to the Sun (Gosling et al., 1987a). Throughout the remainder of the ejecta, electrons stream uni-directionally along field lines, predominantly in the direction opposite to the magnetic field orientation (therefore away from the Sun, from 10 UT on January 22). This beam is nearly always stronger than the other, except between

approximately 5 and 10 UT on January 22, where it is temporarily no longer intercepted by *ACE*. This is difficult to interpret as many different factors may account for the asymmetry in intensity between the beams (see review by Wimmer-Schweingruber et al., 2006). One of those factors is the skewing of closed loops along the Parker spiral, thus biasing the spacecraft interception toward the nearest leg of the loops (Pilipp et al., 1987). These observations suggest that the overlying loops, forming a canopy connected at both ends to the Sun, are followed by the outskirts of a flux rope (according to the interpretation of the MCL) connected initially at both ends and then only at one end to the Sun. The region partly disconnected in the middle of the ejecta may correspond to inner layers of the flux rope. Given the estimated length scale of the ejecta, the overlying loop connected at both ends to the Sun may reach heliospheric distances of the order of 1.25 AU.

5. The ICME in the heliosphere: the MCL-MC connection

To support the interpretation of the MCL in terms of a flux rope, we present briefly in Figure 7 the related plasma and magnetic field in-situ measurements of the ICME, observed at the *Ulysses* spacecraft situated 5.3 AU from the Sun, 17 degrees south of the ecliptic, and 27 degrees from the Sun-Earth line to the west. The magnetic field data is provided by the Vector Helium Magnetometer (VHM) (Balogh et al., 1992). Plasma measurements are provided by the Solar Wind Observations Over the Poles of the Sun (SWOOPS) instrument (Bame et al., 1992). The data series presented are chosen to identify boundaries as in Section 2. In particular, the proton temperature is the lower estimate, 'T-small', calculated to avoid contamination from alpha particles. The expected temperature T_{ex} in Figure 7f is obtained using the well-established correlation (not specific to the *ACE*/SWEPAM instrument) between the proton temperature and the solar wind speed (*e.g.*, Lopez, 1987; Richardson and Cane, 1995), *viz.*

$$T_{ex}[\mathrm{K}] = \begin{cases} (0.031 V_{sw}\,[\mathrm{km\,s^{-1}}] - 5.1)^2 \times 10^3, & V_{sw} < 500\,\mathrm{km\,s^{-1}} \\ (0.51 V_{sw}\,[\mathrm{km\,s^{-1}}] - 142) \times 10^3, & V_{sw} \geq 500\,\mathrm{km\,s^{-1}} \end{cases} .$$

The helium enhancements, as shown in Figure 7h, are considered to be the best preserved ICME signatures, when present, for tracking ICMEs throughout the heliosphere (see von Steiger and Richardson, 2006, for a recent review on ICMEs in the outer heliosphere). The large differences with the helium enhancements near L1 (Figure 3f) may represent spatial variations within the same ICME, consistent with the non-homogeneous, 'raisin-pudding' or lumpy, distribution of helium-rich plasma found in ICMEs (Bame et al., 1979).

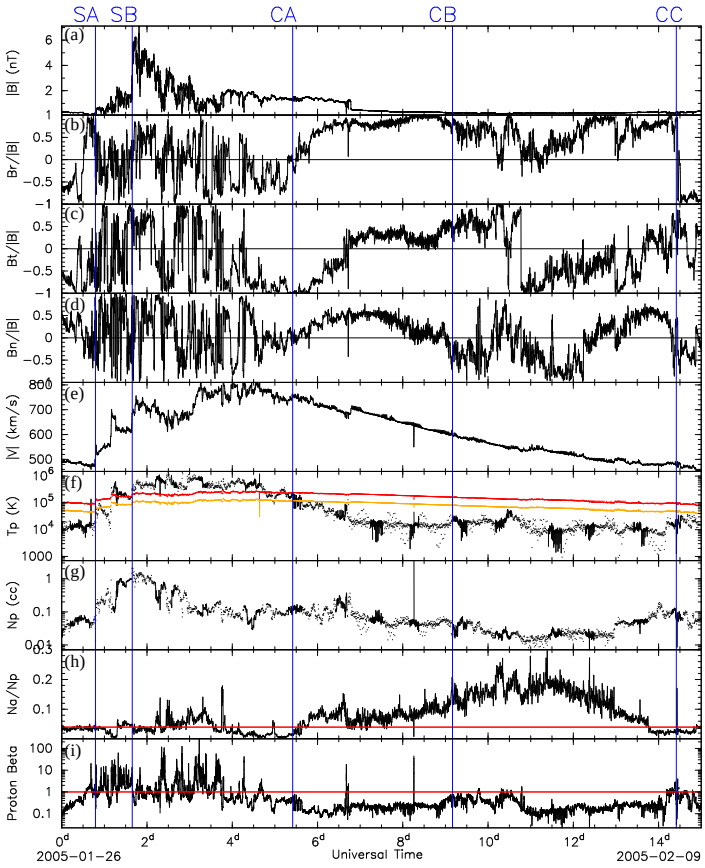

Figure 7. The ICME observed on January 26 – February 9, 2005 by *Ulysses*. The plot shows (a) the magnitude and (b-d) the normalised components of the magnetic field, (e) the plasma (proton) bulk flow speed, (f) the proton temperature (black), the expected temperature T_{ex} (red) computed from the observed solar wind speed and $T_{ex}/2$ (orange), (g) the proton number density, (h) the alpha to proton density ratio, the typical 4% ratio observed in the solar wind (red) and (i) the proton plasma beta (black) and a threshold of 1 (red). With analogy to the ICME observed near Earth, vertical lines indicate the arrival of the shock, SA, the ejecta front, SB, the boundaries, CA and CB, of a possible MC, and the trailing boundary of the ejecta, CC.

Given its strong expansion, we expect to observe a large portion of the ICME near 5.3 AU. With analogy to the ICME observed near L1, boundaries are indicated in Figure 7: the shock SA (19 UT on January 26), the ejecta front boundaries, SB (15:40 UT on January 27), the boundaries, CA and CB, of a possible MC (10 UT on January 31 - 4 UT on February 4) and, in addition, the trailing boundary of a complex ejecta appended to the cloud, CC (10 UT on February 9). As expected, the ICME and its substructures observed by *Ulysses* are much more expanded in time than near the Earth at 1 AU. The full ICME complex takes 14.6 days to pass the spacecraft. The

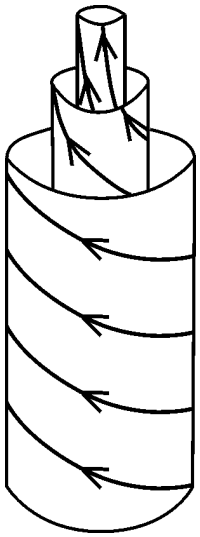

Figure 8. The flux rope of type ENW, when viewed by an observer looking towards the Sun. The magnetic field vector rotates from the east to the north at the flux rope axis and finally to the west at the trailing edge. The rotation is left handed and the axis is perpendicular to the ecliptic plane and orientated towards the north ($\theta_C \sim 90°$).

shock and ejecta speeds near the primary direction of travel of the ICME are expected to be faster than on the flanks. We note that, accordingly, the transit speed of the ICME region between the Sun and *Ulysses* is $\sim$ 1400 $\mathrm{km\,s^{-1}}$, that is 200 $\mathrm{km\,s^{-1}}$faster than the transit speed at L1.

Moreover, in a projection onto the ecliptic plane, we expect to be closer to the primary direction of travel of the ICME. In Figure 7bcd, the magnetic field components are represented in the heliographic Radial Tangential Normal (RTN) system of reference ($\hat{\mathbf{R}}$, $\hat{\mathbf{T}}$, $\hat{\mathbf{N}}$) and normalised. In this coordinate system, $\hat{\mathbf{R}}$ points from the Sun to the spacecraft, $\hat{\mathbf{T}}$ is the Sun's rotation vector crossed into $\hat{\mathbf{R}}$ (thus toward west for a spacecraft near the ecliptic) and $\hat{\mathbf{N}}$ completes the right-handed system (thus toward north for a spacecraft near the ecliptic). At L1, the correspondence between GSE and RTN is thus $B_x \equiv -B_r$, $B_y \equiv -B_t$, $B_z \equiv B_n$ for the magnetic field components. In Figure 7bcd, between CA and CB, we distinguish a clear coherent rotation of the magnetic field vector, coincident with relatively low levels of field-magnitude fluctuations, low proton temperatures (Figure 7f) and low values of proton plasma beta (Figure 7i). These are therefore the signatures of a magnetic cloud. In the first half of the cloud, we note an abrupt change in the magnetic field time series, coinciding with a jump in bulk flow speed and reminiscent of a change in magnetic field intensity found near L1 (see Figure 3, in the first half of the MCL).

Between CA and CB, the magnetic field vector turns from east ($B_t < 0$) to north on the cloud's axis ($B_n > 0$) and finally to the west ($B_t > 0$). Therefore this MC can be classified as an ENW cloud, following the concept proposed by Bothmer and Schwenn (1998). Qualitatively, ENW means a flux rope with the axis orientated towards the north (elevation angle, θ_C, perpendicular to the ecliptic plane) and with left-handed chirality (see Figure 8). The flux rope properties inferred from the observations by *Ulysses* are consistent with the derived axis orientation and the slight signature of axial twisted field ($B_z > 0$, see Figure 6c) near the eastern flank of the cloud at L1.

The clear correspondence between the structures of the ICMEs at L1 and at *Ulysses* demonstrates the connection between MCL and MC and is, aposteriori, evidence that the MCL may be interpreted as the outskirts of a MC. Further comparisons between the observations at *ACE* and *Ulysses* for this event are presented by Rodriguez et al. (2007).

6. Discussion

Figure 9 summarises the observations and is helpful to interpret the global geometry of the ICME observed near Earth. Corresponding solar observations, on January 20, 2005 around 6 UT, are given in Figure 10. They are helpful to confirm the ICME geometry derived from the observations near L1 and at *Ulysses* and serve to understand further its likely formation and evolution in the corona and heliosphere. This includes a magnetogram from the Michelson Doppler Imager (MDI) (Scherrer et al., 1995) onboard the Solar and Heliospheric Observatory (*SoHO*), EUV images from the Transition Region and Coronal Explorer (*TRACE*) (Handy et al., 1999) and the Extreme-Ultraviolet Imaging Telescope (EIT/*SoHO*) (Delaboudinière et al., 1995), and an image from the Large Angle Spectroscopic Coronagraph (LASCO/*SoHO*) (Brueckner et al., 1995).

Traversals by well-separated near-Earth spacecraft provide a coherent picture of the ICME under study, on the spatial scale of the Earth's magnetospheric cross-section. In this case, also, they reveal the presence of an unexpected current sheet substructure. In Section 3, we established the presence, within the leading edge of the ejecta and in the dawn sector, of a tilted current sheet, with normal principally orientated in the north-south direction and across which the IMF component along the Sun-Earth line reverses its sign. In-and-out crossings of the tilted discontinuity in the dawn sector, as observed by *ACE* and *Wind* in the solar wind and later on by *Geotail* in the magnetosheath, define transitions into a region of outward IMF (pink area in Figure 9). This region is not observed by *Cluster* in the dusk sector, where the IMF points inward. In Section 4, we showed that, this substructure aside, the plasma and magnetic observations of the ejecta are

consistent with the outskirts of a structure in strong expansion, with its bulk dawnward of *ACE* and *Wind* and its axis nearly perpendicular to the ecliptic. In Figure 9, the main axis of the interplanetary flux rope is represented as a curved dashed black arrow, with the stronger inner helicoidal fields indicated in blue. These observations suggest that the tilted current sheet is draped within the overlying cloud canopy, ahead of a MCL. The flux rope interpretation of this structure near L1, confirmed by observations of the corresponding MC, provided by *Ulysses* at 5.3 AU and away from the Sun-Earth line, indicate that the bulk of the cloud is in the north-west sector. This is consistent with the primary direction of travel of the fast halo-CME observed at the Sun, as indicated in the LASCO image (Figure 10d), showing that the main bulk of the mass ejection, in the plane of the sky and above the occulting disk in black, is in the north-west sector (see also, Gopalswamy et al., 2005; Simnett, 2006). This north-west direction is also confirmed by observations from the Solar Mass Ejection Imager (*SMEI*) (Jackson, Hick and Buffington, 2006).

In addition to contributing to the near-Earth multi-spacecraft study of the ICME structure and substructure, *Cluster* provides accurate normals and velocities of the driven shock and ejecta fronts, thanks to its 4-spacecraft discontinuity analysis capability. The ejecta axis, perpendicular to the shock and ejecta front normals, is consistent with the cloud driving the shock. However, the normals of the driven shock SA and of the ejecta front SB have slightly different directions away from the Sun-Earth line (Section 3). In Section 4, we showed that the ejecta is in strong expansion, with the expansion direction towards the east and south. This is consistent with the direction of the normals SB1-SB2, pointing slightly towards the south. Therefore the ejecta front, SB, behind the driven shock SA, may be attributed to the expansion and evolution of the ejecta, towards the east and south, while the fast driven shock SA maintains a north-west orientation, consistent with the primary direction of the cloud (see normals indicated by blue arrows in Figure 9). To our knowledge, this is the first reported observation of a difference between the shock and the ejecta normals. Whereas such a difference is not expected near the primary front edge of an ICME, it is reasonable to find that shock and ejecta normals can differ at the flank of a cloud expanding sideways. This observation also corroborates the differences in accelerations, observed by Rust et al. (2005) in LASCO coronagraph images, between the faint features of CME leading edges, imputed to overlying loops, and CME bright knots that presumably entrain flux ropes. Thus, the ejecta front is considered to form an overlying canopy of field lines ahead of the flux rope and may be attributed to fields and mass from the background corona swept up into motion by the rising flux rope, as suggested by Illing and Hundhausen (1985). This would explain why the propagation direction of the ejecta front

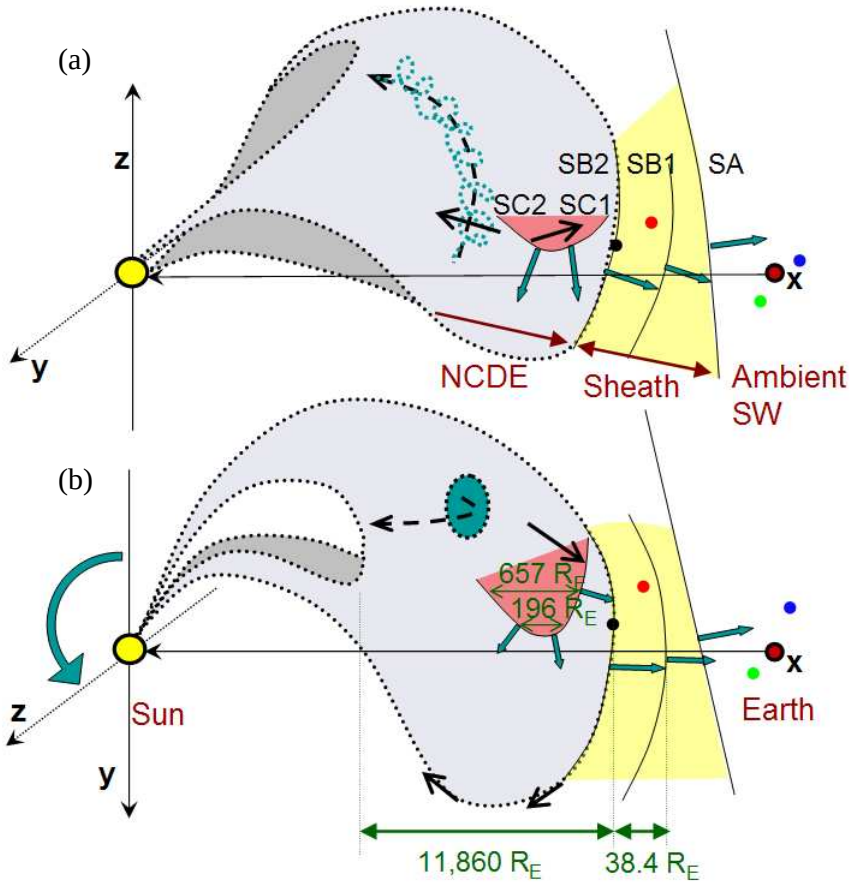

Figure 9. Possible interpretation of the global geometry of the ICME observed on January 21-22, 2005 near L1. The ICME shock front, sheath and ejecta are projected on (a) the noon-midnight meridional plane and (b) the ecliptic plane (in the GSE Cartesian coordinate system), with perspective rendered in dark grey. Scales in the $\hat{\mathbf{X}}_{GSE}$ direction are shrinking (with time). *Wind*, *ACE*, *Cluster* and *Geotail* are indicated by circles filled in black, red, green and blue respectively. The yellow and blue grey areas represent the sheath and the ejecta, respectively. Discontinuity normals are indicated with blue arrows. IMF orientations observed or inferred at different locations in the ejecta are indicated with plain black arrows. A curved dashed black arrow represents the main axis of the interplanetary flux rope, with the stronger inner helicoidal fields indicated in blue. The counter-clockwise rotation of the corresponding coronal flux rope axis is indicated by a blue rounded arrow in (b).

on the flank is connected to the flow deflections inside the leading ejecta and not to the primary direction of the cloud.

The presence of the NCDE and the helium enrichment at the leading edge of the ejecta could help to identify the possible scenario for the formation or evolution of the CME. In Section 2, we showed that the NCDE

is caused essentially by an enrichment in helium. The helium enrichment may be attributed to the arrival of 'flare driver gas' (*e.g.*, Hirshberg, Bame and Robbins, 1972; Bame et al., 1979). This agrees with the position near the streamer belt of the flaring active region NOAA 10720 (x-ray GOES level X7.1) associated with the CME. Lower coronal observations of the event show that, prior to the eruption, the filament associated with the CME (not shown) was aligned east-west along a magnetic neutral line. Predominantly bipolar fields, seen in magnetograms (Figure 10a; see also Zhang, 2007), point inward and outward, respectively above and below this neutral line nearly parallel to the ecliptic plane, in accordance with the global heliospheric magnetic configuration. Indeed, in this period of solar minimum (between solar cycle maxima in 2001 and 2012), the inward IMF is connected to the northern solar magnetic hemisphere, and the outward IMF to the southern hemisphere. The eruption of the filament is confirmed also by the observation of the two-ribbon flare occurring either side of the neutral line; see Figure 10b.

Counter-streaming suprathermal electrons, observed in the first half of the ejecta passage, are interpreted as signatures of nested magnetic loops overlying the flux rope, which are still connected to the Sun. However, the magnetic field direction of those loops, which are thought to belong to the cloud southern flank, are of inward IMF type ($B_x > 0$), and are therefore expected to be connected to the northern hemisphere in that period of the solar cycle, as explained previously. Moreover, there is a large difference in orientation between the interplanetary flux rope axis and the axis of the coronal arcade and filament (along the neutral line) on the solar surface. The curved axis of the neutral line is found to be orientated within $10 \pm 15°$ with respect to the ecliptic. This estimate is based on observations taken, for instance on January 17, when the region is closer to the centre of the disk, prior to the eruption. Such observations are devoid of projection effects, contrary to the Figures 10ab where the westernmost, inclined portion of the axis dominates. This estimate takes also into account a correction angle due to the inclination between equatorial and ecliptic planes (the effect being stronger towards the limbs). The inconsistencies between the interplanetary and solar observations indicate that the overlying arcade of loops connected to the Sun is highly rotated, by about $80 \pm 15°$.

Such differences in the orientation of the flux rope at the Sun and in interplanetary space have been reported previously (Rust et al., 2005; Wang et al., 2006). Possibly related are the differences between the central positions of the source regions and three-part structured CMEs observed on the limb; these differences could be attributed, in the rising phase of solar activity, to equatorward deflections of the CMEs by the fast solar wind emanating from neighbouring coronal holes (Cremades and Bothmer, 2004). However, such deflections do not necessarily imply a change in the inclina-

tion of the CME axis. In fact, in the rising phase of the solar cycle, MCs are frequently observed with their axis highly inclined with respect to the ecliptic ($\theta_C > 45°$) (Huttunen et al., 2005). In the present case, it is not possible to infer the axis orientation or direction of rotation, if any, from the available observations of the (halo) CME. Nevertheless, there is more and more evidence that the axial rotation of erupting filaments is happening in the solar corona (Rust, 2003; Rust and LaBonte, 2005; Williams et al., 2005; Zhou et al., 2006).

One plausible explanation for this flux rope rotation is that the eruption at the Sun involved the helical kink instability (Török, Kliem and Titov, 2004). This MHD instability occurs when the twist in a flux rope exceeds a critical value. In particular, simulations predict a rotation angle of the flux rope axis ranging between 100 and 140° (Török, private communication; see also Fan and Gibson, 2003, 2004; Török and Kliem, 2003, 2005). The direction of rotation (*i.e.* clockwise or anti-clockwise) depends on the sign of magnetic helicity in the region, which provides the sense of twist in the magnetic flux rope. Magnetic helicity quantifies how the magnetic field is sheared and twisted compared to its lowest energy state (potential field) (see Démoulin, 2007, for a recent review). The simulations indicate that flux ropes with right (left) handed twist rotate clockwise (counter-clockwise) whilst undergoing the kink instability. Recent work by Green et al. (2007) shows that filaments observed to rotate upon eruption follow this rule.

The active region associated with the CME contains negative magnetic helicity, as derived from magnetograms by Zhang (2007). For the time period between January 12 and 18, Zhang (2007) derived an estimated magnetic helicity $H_m \sim -2 \times 10^{43}\mathrm{Mx}^2$, attributed to the emergence of highly sheared magnetic flux near the neutral line. The reverse 'S' shape of the EUV ribbons seen in *TRACE* data after the flux rope eruption on January 20 (see Figure 10b) is also indicative of negative magnetic helicity. Titov and Démoulin (1999) showed that, under a flux rope, separatrix surfaces form, which trace out a forward (reverse) 'S' shape at their chromospheric footprints for flux ropes with right-handed (left-handed) twist. Upon eruption, energy release occurs in these regions and results in the flare ribbons. Therefore we conclude that the flux rope had left-handed (or negative) twist, which implies that the solar flux rope should rotate anti-clockwise upon eruption.

The left-handed twist (negative helicity) of the coronal flux rope and the photospheric magnetic configuration imply a flux rope axis directed towards the west. We showed in Section 5 that the associated interplanetary flux rope is of the same chirality (left-handed), consistent with helicity conservation in the ejected flux rope from the corona (Bothmer and Rust, 1997). The interplanetary flux rope is orientated towards the north (in the $\hat{\mathbf{Z}}_{GSE}$ positive direction). Thus, the analysis of solar and interplanetary observations yields a counter-clockwise rotation angle of 80° for the ejected flux rope,

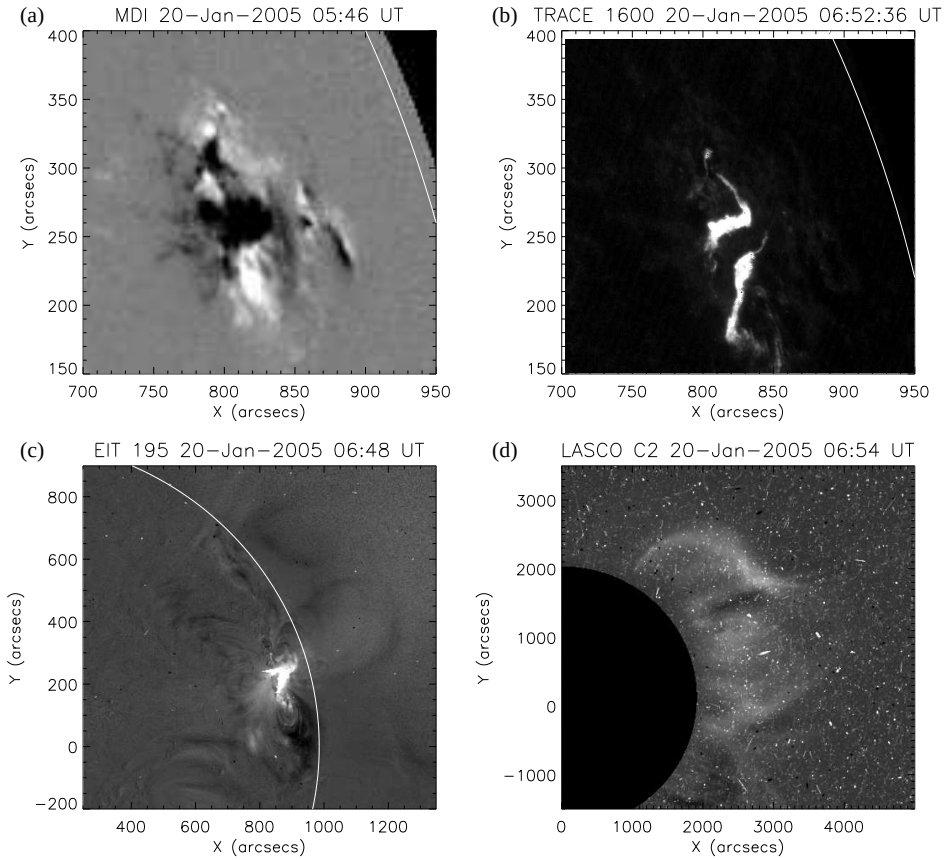

Figure 10. North-west quadrants of the Sun on January 20, 2005 around 6 UT. (a) MDI magnetogram before eruption. White and black intensity levels indicate positive (outward) and negative (inward) polarities, respectively. (b) *TRACE* 1600Å image of the flare ribbons after eruption. (c) EIT 195Å running difference image at the time of the eruption, showing dimming regions that extend outside of the active region (d) LASCO C2 coronagraph, with the occulting disc in black, indicating the primary direction of travel of the fast halo CME in the plane of the sky, *i.e.* towards the north-west. In panels a, b and c, the position of the solar limb is indicated by a white arc.

consistent with the theoretically-predicted angle in the case of helical kink instability. The counter-clockwise rotation of the flux rope axis is indicated near the Sun by twisted arcade footpoints in Figure 9a and a blue rounded arrow in Figure 9b. It is thus possible to envisage that the erupting flux rope, subject to a helical kink instability, drags the overlying arcade with a rotation, thereby changing the topological magnetic configuration between the arcade and the streamer belt. This is consistent with observations in the solar corona (Figure 10c) showing that the spatial scale of the CME is much bigger than the flaring active region. This scenario would explain

the rotation of the flux rope axis and the cloud polarities opposite to the expected ambient IMF.

One hypothesis for the formation of the current sheet substructure could involve the interaction of the ICME with the trailing edge of a slower ICME (560 $\mathrm{km\,s^{-1}}$ before shock). However, such interaction would result in the formation of a fast complex ejecta, with characteristics that differ from those of MCs (Burlaga et al., 2001). The current sheet substructure may also correspond to a remnant current sheet formed in the complex active region NOAA 10720, and dragged along between the flux rope and the overlying arcade. Such current sheet could probably form above the multi-polar magnetic region shown in Figure 10a. The formation of this current sheet may also be related to the eruption at the Sun. However, without observations that fully trace the erupting structure, the formation of the current sheet and its relation with the CME onset and evolution is difficult to determine.

The connection between MC and MCL, as demonstrated for the same event in Sections 4 and 5, is of importance to interpret solar cycle variations in the fraction of ICMEs identified as MCs at 1 AU. The fraction varies from roughly 100% near times of solar minimum to about 15% around solar maximum (Richardson and Cane, 2004b). However, about half of ICMEs may represent MCLs (Cane and Richardson, 2003). Wu, Lepping and Gopalswamy (2006) suggest that the solar sources (*e.g.* associated prominence eruptions) of MCLs are located at higher heliolatitudes for those events. In the present case, the solar event location (N14W67 for the NOAA 10720) supports this interpretation, but also suggests that the solar sources of MCLs might be found at distant heliolongitudes. The available in-situ observations in the heliosphere limit the longitudinal extent of the cloud to a minimum of 27°. However, the longitude of the solar event location corresponds to a longitudinal half-extent at 1 AU, *i.e.* 67°, that scores off the upper limit of $\sim 50°$ reported so far (*e.g.*, Borrini et al., 1982; Cane and Richardson, 2003).

Although the magnetic cloud is not exactly Earth-directed, consequences for the Earth's magnetosphere are not avoided due to the expansion of the ejecta towards Earth. The interaction of the ICME with the Earth's magnetosphere operates essentially through the increase in solar wind speed and the southward IMF conditions associated with the ICME shock and sheath. Not discussed here are the individual effects due to the current sheet substructure within the cloud ejecta. Since its normal is principally orientated in the north-south direction, the tilted current sheet on the dawn side may generate a hot flow anomaly (HFA) as it intersects the bow shock (Schwartz et al., 2000; Eastwood et al., 2005). Such HFA is expected to lead to the outward expansion of the bow shock, due to the formation of a bulge on its surface and could explain pressure variations (observed by

Geotail, see Section 3.1) and a foreshock sunward motion (resulting in the entry of *Cluster* into the foreshock ULF wave field, see Figure 5). Further investigation on this aspect is beyond the scope of this paper and will be published elsewhere.

To sum up briefly, the main features of this multi-spacecraft ICME study are: (a) the rare identification of a magnetic cloud on its flank, with the largest longitudinal half-extent observed so far (67°); (b) differences between the shock and ejecta normals, consistent with the cloud expansion on its flank; (c) a NCDE caused by an enrichment in helium at the ejecta front; (d) a large ($\sim$ 80°) rotation of the flux rope and the overlying arcade (or cloud canopy), consistent with the flux rope being subject to the helical kink instability at the Sun; (e) an unexpected current sheet substructure dragged along between the flux rope and the overlying cloud canopy.

Acknowledgements

The authors are grateful to L.K. Harra for organising the Sun-Earth Connection workshop at MSSL, with funds from a Phillip Leverhulm Prize, from which this contribution is an outcome. C.F. would like to thank L. van Driel-Gesztelyi, T. Török and P. Démoulin for helpful discussions. C.F. and Y.V.B. acknowledge financial support from the UK Particle Physics and Astronomy Research Council (PPARC) on the MSSL Rolling Grant. S.D. is supported by the Argentinean grants UBACyT X329, PIP 6220 (CONICET) and PICT 03-14163 (ANPCyT). S.D. is a member of the Carrera del Investigador Científico, CONICET. L.M.G. acknowledges the Royal Society for postdoctoral research funding. N.U.C. acknowledges the US National Science Foundation grant ATM-0553397.

We acknowledge use of *Wind*, *ACE*, *Cluster*, *Geotail* and *Ulysses* data from magnetic field and plasma in-situ experiments. We thank their respective Principal Investigators, namely R.P. Lepping (*Wind*/MFI), N.F. Ness (*ACE*/MAG), D.J. McComas (*ACE*/SWEPAM and *Ulysses*/SWOOPS), E. Lucek (*Cluster*/FGM), H. Rème (*Cluster*/CIS), S. Kokubun (*Geotail*/MGF), L.A. Frank (*Geotail*/CPI) and A. Balogh (*Ulysses*/VHM). This research has made use of NASA's Space Physics Data Facility (SPDF). *TRACE* is a mission of the Stanford-Lockheed Institute for Space Research, and part of the NASA Small Explorer program. MDI, EIT and LASCO data are courtesy of *SoHO* consortia; *SoHO* is a project of international cooperation between ESA and NASA.

References

Balogh, A., Beek, T. J., Forsyth, R. J., Hedgecock, P. C., Marquedant, R. J., Smith, E. J., et al.: 1992, *Astron. Astrophys. Suppl. Ser.* **92**, 221.

Balogh, A., Carr, C. M., Acuña, M. H., Dunlop, M. W., Beek, T. J., Brown, P., et al.: 2001, *Ann. Geophys.* **19**, 1207.

Bame, S. J., Asbridge, J. R., Feldman, W. C., Fenimore, E. E., and Gosling, J. T.: 1979, *Solar Phys.* **62**, 179.

Bame, S. J., McComas, D. J., Barraclough, B. L., Phillips, J. L., Sofaly, K. J., Chavez, J. C., et al.: 1992, *Astron. Astrophys. Suppl. Ser.* **92**, 237.

Borrini, G., Gosling, J. T., Bame, S. J., and Feldman, W. C.: 1982, *J. Geophys. Res.* **87**, 7370.

Bothmer, V. and Rust, D. M.: 1997, in N. U. Crooker, J. A. Joselyn, and J. Feynman (ed.), *Coronal Mass Ejections*, Geophys. Monogr. Ser., vol. 99, American Geophysical Union, Washington DC, p. 139.

Bothmer, V. and Schwenn, R.: 1998, *Ann. Geophys.* **16**, 1.

Brueckner, G. E., Howard, R. A., Koomen, M. J., Korendyke, C. M., Michels, D. J., Moses, J. D., et al.: 1995, *Solar Phys.* **162**, 357.

Burlaga, L. F.: 2001, *Eos Trans. AGU* **82**, 433.

Burlaga, L. F., Sittler, E., Mariani, F., and Schwenn, R.: 1981, *J. Geophys. Res.* **86**, 6673.

Burlaga, L. F., Skoug, R. M., Smith, C. W., Webb, D. F., Zurbuchen, T. H., and Reinard, A.: 2001, *J. Geophys. Res.* **106**, 20957.

Cane, H. V. and Richardson, I. G.: 2003, *J. Geophys. Res.* **108**(A4), 1156.

Cremades, H. and Bothmer, V.: 2004, *Astron. Astrophys.* **422**, 307.

Crooker, N. U. and Webb, D. F.: 2006, *J. Geophys. Res.* **111**(A10), 8108.

Dasso, S., Mandrini, C. H., Démoulin, P., Luoni, M. L., and Gulisano, A. M.: 2005, *Adv. Space Res.* **35**, 711.

Dasso, S., Mandrini, C. H., Démoulin, P., and Luoni, M. L.: 2006, *Astron. Astrophys.* **455**, 349.

Delaboudinière, J.-P., Artzner, G. E., Brunaud, J., Gabriel, A. H., Hochedez, J. F., Millier, F., et al.: 1995, *Solar Phys.* **162**, 291.

Démoulin, P.: 2007, *Adv. Space Res.*, in press.

Eastwood, J. P., Lucek, E. A., Mazelle, C., Meziane, K., Narita, Y., Pickett, J., et al.: 2005, *Space Sci. Rev.* **118**, 41.

Fairfield, D. H.: 1971, *J. Geophys. Res.* **76**, 6700.

Fan, Y. and Gibson, S. E.: 2003, *Astrophys. J.* **589**, L105.

Fan, Y. and Gibson, S. E.: 2004, *Astrophys. J.* **609**, 1123.

Farrugia, C. J., Dunlop, M. W., Geurts, F., Balogh, A., Southwood, D. J., Bryant, D. A., et al.: 1990, *Geophys. Res. Lett.* **17**, 1025.

Fazakerley, A. N., Harra, L. K., Culhane, J. L., van Driel-Gesztelyi, L., Lucek, E., Matthews, S. A., et al.: 2005, *Geophys. Res. Lett.* **32**, 13105.

Forbes, T. G., Linker, J. A., Chen, J., Cid, C., Kóta, J., Lee, M. A., et al.: 2006, *Space Sci. Rev.* **123**, 251.

Forsyth, R. J., Bothmer, V., Cid, C., Crooker, N. U., Horbury, T. S., Kecskemety, K., et al.: 2006, *Space Sci. Rev.* **123**, 383.

Frank, L. A., Ackerson, K. L., Paterson, W. R., Lee, J. A., English, M. R., and Pickett, G. L.: 1994, *J. Geomag. and Geoelectr.* **46**, 23.

Galvin, A. B., Ipavich, F. M., Gloeckler, G., Hovestadt, D., and Tsurutani, B. T.: 1987, *J. Geophys. Res.* **92**, 12069.

Gonzalez, W. D. and Tsurutani, B. T.: 1987, *Planet. Space Sci.* **35**, 1101.

Gopalswamy, N., Xie, H., Yashiro, S., and Usoskin, I.: 2005, in *29th International Cosmic Ray Conference (Pune)*, p. 169.
Gosling, J. T.: 1990, in C. T. Russell, E. R. Priest, and L. C. Lee (ed.), *Physics of Magnetic Flux Ropes*, Geophys. Monogr. Ser., vol. 58, American Geophysical Union, Washington DC, p. 343.
Gosling, J. T. and McComas, D. J.: 1987, *Geophys. Res. Lett.* **14**, 355.
Gosling, J. T., Asbridge, J. R., Bame, S. J., Feldman, W. C., and Hildner, E.: 1977, *J. Geophys. Res.* **82**, 5005.
Gosling, J. T., Baker, D. N., Bame, S. J., Feldman, W. C., Zwickl, R. D., and Smith, E. J.: 1987a, *J. Geophys. Res.* **92**, 8519.
Gosling, J. T., Thomsen, M. F., Bame, S. J., and Zwickl, R. D.: 1987b, *J. Geophys. Res.* **92**, 12399.
Green, L. M., Kliem, B., Török, T., van Driel-Gesztelyi, L., and Attrill, G.: 2007, *Solar Phys.*, submitted.
Gulisano, A. M., Dasso, S., Mandrini, C. H., and Démoulin, P.: 2005, in *ESA SP-592: Solar Wind 11/SOHO 16, Connecting Sun and Heliosphere*, p. 621.
Handy, B. N., Acton, L. W., Kankelborg, C. C., Wolfson, C. J., Akin, D. J., Bruner, M. E., et al.: 1999, *Solar Phys.* **187**, 229.
Hirshberg, J., Bame, S. J., and Robbins, D. E.: 1972, *Solar Phys.* **23**, 467.
Hu, Q. and Sonnerup, B. U. Ö.: 2001, *Geophys. Res. Lett.* **28**, 467.
Huttunen, K. E. J., Schwenn, R., Bothmer, V., and Koskinen, H. E. J.: 2005, *Ann. Geophys.* **23**, 625.
Illing, R. M. E. and Hundhausen, A. J.: 1985, *J. Geophys. Res.* **90**, 275.
Jackson, B. V., Hick, P. P., and Buffington, A.: 2006, *AGU Fall Meeting Abstracts*, A396.
Jones, G. H., Rees, A., Balogh, A., and Forsyth, R. J.: 2002, *Geophys. Res. Lett.* **29**, 15.
Kokubun, S., Yamamoto, T., Acuna, M. H., Hayashi, K., Shiokawa, K., and Kawano, H.: 1994, *J. Geomag. and Geoelectr.* **46**, 7.
Lepping, R. P., Burlaga, L. F., and Jones, J. A.: 1990, *J. Geophys. Res.* **95**, 11957.
Lepping, R. P., Wu, C.-C., and Berdichevsky, D. B.: 2005, *Ann. Geophys.* **23**, 2687.
Lepping, R. P., Acuna, M., Burlaga, L., Farrell, W., Slavin, J., Schatten, F., et al.: 1995, *Space Sci. Rev.* **71**, 207.
Lepping, R. P., Berdichevsky, D. B., Burlaga, L. F., Lazarus, A. J., Kasper, J., Desch, M. D., et al.: 2001, *Solar Phys.* **204**, 285.
Lepping, R. P., Berdichevsky, D. B., Szabo, A., Arqueros, C., and Lazarus, A. J.: 2003, *Solar Phys.* **212**, 425.
Lopez, R. E.: 1987, *J. Geophys. Res.* **92**, 11189.
Mandrini, C. H., Pohjolainen, S., Dasso, S., Green, L. M., Démoulin, P., van Driel-Gesztelyi, L., et al.: 2005, *Astron. Astrophys.* **434**, 725.
Marubashi, K.: 1986, *Adv. Space Res.* **6**, 335.
Marubashi, K.: 1997, in N. U. Crooker, J. A. Joselyn, and J. Feynman (ed.), *Coronal Mass Ejections*, Geophys. Monogr. Ser., vol. 99, American Geophysical Union, Washington DC, p. 147.
McComas, D. J., Gosling, J. T., Winterhalter, D., and Smith, E. J.: 1988, *J. Geophys. Res.* **93**, 2519.
McComas, D. J., Bame, S. J., Barker, P., Feldman, W. C., Phillips, J. L., Riley, P., et al.: 1998, *Space Sci. Rev.* **86**, 563.
Mewaldt, R. A., Looper, M. D., Cohen, C. M. S., Mason, G. M., Haggerty, D. K., Desai, M. I., et al.: 2005, in *29th International Cosmic Ray Conference (Pune)*, p. 101.
Mullan, D. J. and Smith, C. W.: 2006, *Solar Phys.* **234**, 325.
Mullan, D. J., Smith, C. W., Ness, N. F., and Skoug, R. M.: 2003, *Astrophys. J.* **583**, 496.

Neugebauer, M. and Goldstein, R.: 1997, in N. U. Crooker, J. A. Joselyn, and J. Feynman (ed.), *Coronal Mass Ejections*, Geophys. Monogr. Ser., vol. 99, American Geophysical Union, Washington DC, p. 245.
Neugebauer, M., Clay, D. R., and Gosling, J. T.: 1993, *J. Geophys. Res.* **98**, 9383.
Neugebauer, M., Steinberg, J. T., Tokar, R. L., Barraclough, B. L., Dors, E. E., Wiens, R. C., et al.: 2003, *Space Sci. Rev.* **105**, 661.
Ogilvie, K. W., Chornay, D. J., Fritzenreiter, R. J., Hunsaker, F., Keller, J., Lobell, J., et al.: 1995, *Space Sci. Rev.* **71**, 55.
Owens, M. J. and Cargill, P. J.: 2004, *Ann. Geophys.* **22**, 4397.
Owens, M. J., Cargill, P. J., Pagel, C., Siscoe, G. L., and Crooker, N. U.: 2005, *J. Geophys. Res.* **110**(A9), 1105.
Pilipp, W. G., Muehlhaeuser, K.-H., Miggenrieder, H., Rosenbauer, H., and Schwenn, R.: 1987, *J. Geophys. Res.* **92**, 1103.
Rème, H., Aoustin, C., Bosqued, J. M., Dandouras, I., Lavraud, B., Sauvaud, J. A., et al.: 2001, *Ann. Geophys.* **19**, 1303.
Richardson, I. G. and Cane, H. V.: 1995, *J. Geophys. Res.* **100**, 23397.
Richardson, I. G. and Cane, H. V.: 2004a, *J. Geophys. Res.* **109**, 9104.
Richardson, I. G. and Cane, H. V.: 2004b, *Geophys. Res. Lett.* **31**, 18804.
Rodriguez, L., Zhukov, A., Dasso, S., Mandrini, C. H., Cremades, H., Cid, C., et al.: 2007, *Ann. Geophys.*, in preparation.
Roelof, E. C. and Sibeck, D. G.: 1993, *J. Geophys. Res.* **98**, 21421.
Russell, C. T. and Shinde, A. A.: 2005, *Solar Phys.* **229**, 323.
Rust, D. M.: 2003, *Adv. Space Res.* **32**, 1895.
Rust, D. M. and LaBonte, B. J.: 2005, *Astrophys. J.* **622**, L69.
Rust, D. M., Anderson, B. J., Andrews, M. D., Acuña, M. H., Russell, C. T., Schuck, P. W., et al.: 2005, *Astrophys. J.* **621**, 524.
Scherrer, P. H., Bogart, R. S., Bush, R. I., Hoeksema, J. T., Kosovichev, A. G., Schou, J., et al.: 1995, *Solar Phys.* **162**, 129.
Schwartz, S. J.: 1998, in G. Pashmann and P. W. Daly (eds.), *Analysis Methods for Multi-Spacecraft Data*, ISSI Scientific Report SR-001, Bern, p. 249.
Schwartz, S. J., Paschmann, G., Sckopke, N., Bauer, T. M., Dunlop, M., Fazakerley, A. N., et al.: 2000, *J. Geophys. Res.* **105**, 12639.
Schwenn, R.: 2006, *Living Rev. Solar Phys.* **3**, URL (cited on August 9, 2006): `http://www.livingreviews.org/lrsp-2006-2`.
Simnett, G. M.: 2006, *Astron. Astrophys.* **445**, 715.
Smith, C. W., L'Heureux, J., Ness, N. F., Acuña, M. H., Burlaga, L. F., and Scheifele, J.: 1998, *Space Sci. Rev.* **86**, 613.
Sonnerup, B. U. Ö. and Scheible, M.: 1998, in G. Pashmann and P. W. Daly (eds.), *Analysis Methods for Multi-Spacecraft Data*, ISSI Scientific Report SR-001, Bern, p. 185.
Szabo, A., Lepping, R. P., Merka, J., Smith, C. W., and Skoug, R. M.: 2001, in B. Battrick, H. Sawaya-Lacoste, E. Marsch, V. Martinez Pillet, B. Fleck, and R. Marsden (eds.), *ESA SP-493: Solar Encounter: the First Solar Orbiter Workshop*, p. 383.
Titov, V. S. and Démoulin, P.: 1999, *Astron. Astrophys.* **351**, 707.
Török, T. and Kliem, B.: 2003, *Astron. Astrophys.* **406**, 1043.
Török, T. and Kliem, B.: 2005, *Astrophys. J.* **630**, L97.
Török, T., Kliem, B., and Titov, V. S.: 2004, *Astron. Astrophys.* **413**, L27.
Tsurutani, B. T., Gonzalez, W. D., Zhou, X.-Y., Lepping, R. P., and Bothmer, V.: 2004, *J. Atmosph. Solar-Terr. Phys.* **66**, 147.
Tylka, A. J.: 2006, `http://creme96.nrl.navy.mil/20Jan05/`, 2006 SHINE Workshop (Utah).

Vallat, C., Dandouras, I., Escoubet, P., Rème, H., Cao, J., Balogh, A., et al.: 2005, *AOGS (Singapore) Conference Communication*, 58–ST–A0590.
von Steiger, R. and Richardson, J. D.: 2006, *Space Sci. Rev.* **123**, 111.
Wang, Y., Zhou, G., Ye, P., Wang, S., and Wang, J.: 2006, *Astrophys. J.* **651**, 1245.
Webb, D. F., Lepping, R. P., Burlaga, L. F., DeForest, C. E., Larson, D. E., Martin, S. F., et al.: 2000, *J. Geophys. Res.* **105**, 27251.
Williams, D. R., Török, T., Démoulin, P., van Driel-Gesztelyi, L., and Kliem, B.: 2005, *Astrophys. J.* **628**, L163.
Wimmer-Schweingruber, R. F., Crooker, N. U., Balogh, A., Bothmer, V., Forsyth, R. J., Gazis, P., et al.: 2006, *Space Sci. Rev.* **123**, 177.
Wu, C.-C., Lepping, R. P., and Gopalswamy, N.: 2003, in A. Wilson (ed.), *ESA SP-535: Solar Variability as an Input to the Earth's Environment*, p. 429.
Wu, C. C., Lepping, R. P., and Gopalswamy, N.: 2006, *Solar Phys.* **239**, 449.
Zhang, H.: 2007, in *ASP Conference Series, 6th SolarB meeting (Kyoto)*, in press.
Zhao, X. P. and Hoeksema, J. T.: 1997, *Geophys. Res. Lett.* **24**, 2965.
Zhou, G. P., Wang, J. X., Zhang, J., Chen, P. F., Ji, H. S., and Dere, K.: 2006, *Astrophys. J.* **651**, 1238.